ORIGINAL RESEARCH ARTICLE

The Effect of Alumina Activity on Dissolution Behavior of Alumina Particles in $CaO–Al_2O_3–SiO_2$ Slags

SANGROK YEO, HYUNGSIC UM, and YONGSUG CHUNG

This study investigated the dissolution of Al_2O_3 particles in $CaO–Al_2O_3–SiO_2$ slag by the single hot thermocouple technique (SHTT) in the temperature range between 1550 °C and 1650 °C. The Al_2O_3 content in slags with basicity (CaO/SiO_2 ratio) fixed at 1 varied from 5 to 35 pct. The evolution of the particle radius over time was obtained by image analysis. In the results of our experiments, the dissolution rate of the Al_2O_3 particles was increased with increasing Al_2O_3 activity in the slag. The rotation of the particle was observed during the dissolution experiment. We used a kinetic model that considered the fluid flow to understand the dissolution phenomenon. We calculated the diffusion coefficient of Al_2O_3 from 10^{-13} to 10^{-10} m^2/s and in a similar manner as in a previous study. The activation energy of Al_2O_3 was 323 kJ/mole at 5 wt pct Al_2O_3, 343 kJ/mole at 20 wt pct Al_2O_3, and to 486 kJ/mole at 35 wt pct Al_2O_3.

https://doi.org/10.1007/s11663-021-02309-0

I. INTRODUCTION

Al_2O_3 inclusions formed in the steelmaking process are produced by the Al deoxidizer added for de-oxidation of molten steel. Generally, the non-metallic inclusions create problems in steelmaking process: for example, nozzle clogging, degradation of the mechanical properties of the product, and degradation weldability.[1–3] The inclusion content should be minimized by removing inclusions from molten steel to a slag. This process involves (1) transport of the inclusion to the interface, (2) separation of the inclusion to the interface, and (3) removal of the inclusion.[4] The final step involves the dissolution of the inclusion particle in the slag. When an inclusion is not quickly dissolved by the slag, the undissolved inclusion near the interface might be re-entertained in the molten steel. Therefore, the dissolution of inclusions is an important phenomenon to make clean steel.

A number of studies to understand dissolution behavior have been carried out by the rotating cylinder method (RCM),[5–11] confocal scanning laser microscopy (CSLM),[4,12–18] and single hot thermocouple technique (SHTT).[19–21] Cooper *et al.*[5] and Choi *et al.*[6] observed the dissolution of alumina in slag with the RCM. They reported that the dissolution of alumina rods was controlled by mass transfer of alumina into $CaO–Al_2O_3–SiO_2$ slag. Taira *et al.*[7] and Bui *et al.*[10] reported using the RCM in which the dissolution rate of Al_2O_3 inclusions was controlled by mass transport of alumina into $CaO–Al_2O_3–SiO_2$ slag. Especially in the study of Bui *et al.*, they observed the formation of intermediate compounds ($CaO{\cdot}2Al_2O_3$, $CaO{\cdot}6Al_2O_3$, $2CaO{\cdot}Al_2O_3{\cdot}SiO_2$) at the particle/slag which could suppress the diffusion of Al_2O_3. Sridhar and Cramb[4] researched the dissolution of Al_2O_3 particles into $CaO–Al_2O_3–SiO_2–MgO$ slag using CSLM. They reported that the dissolution of Al_2O_3 particles was controlled by boundary layer diffusion of alumina in the Stokes regime. Liu *et al.*[13] proposed a new approach using a diffusion equation coupled with Lattice Boltzmann modeling. Using mathematical simulations, the dissolution mechanism at the dissolution of spherical Al_2O_3 particles could be identified as diffusion controlled in $CaO–Al_2O_3–SiO_2$ slag. Michelic *et al.*[17] reported that the dissolution studies including the determination of dissolution mechanisms according to the approach proposed by Liu *et al.*[13] using CSLM is shown for two different slag/inclusion systems. Slag viscosity is a significant factor in both systems, and the shape of the dissolution curve varies with slag viscosity. Generally, the SHTT was used to study the solidification

SANGROK YEO and YONGSUG CHUNG are with the Department of Advanced Materials Engineering, Korea Polytechnic University, 237, Sangidaehak-ro, Shiheung-si, Gyeonggi-do, 15073, Republic of Korea. Contact e-mail: ychung@kpu.ac.kr HYUNGSIC UM is with the Department of Advanced Materials Engineering, Korea Polytechnic University and R&D Center, Dongkuk Steel Company, 70, Geonposaneop-ro 3214beon-gil, Daesong-myeon, Nam-gu, Pohang-si, Gyeongsangbuk-do, 37874, Republic of Korea.
Manuscript submitted April 19, 2021, accepted August 21, 2021.
Article published online September 10, 2021.

Table I. Composition and Weight of an Al_2O_3 Sphere Sample

Type	Source	Weight (mg)	Concentration Al_2O_3 (Pct)	Other (Pct)
Alumina Sphere	goodfellow	0.25	99.9	0.1

Table II. Chemical Composition and Viscosity of Slags

	CaO (Wt pct)	SiO_2 (Wt Pct)	Al_2O_3 (Wt Pct)	Basicity
Slag 1	47.5	47.5	5.0	1
Slag 2	40.0	40.0	20.0	1
Slag 3	32.5	32.5	35.0	1

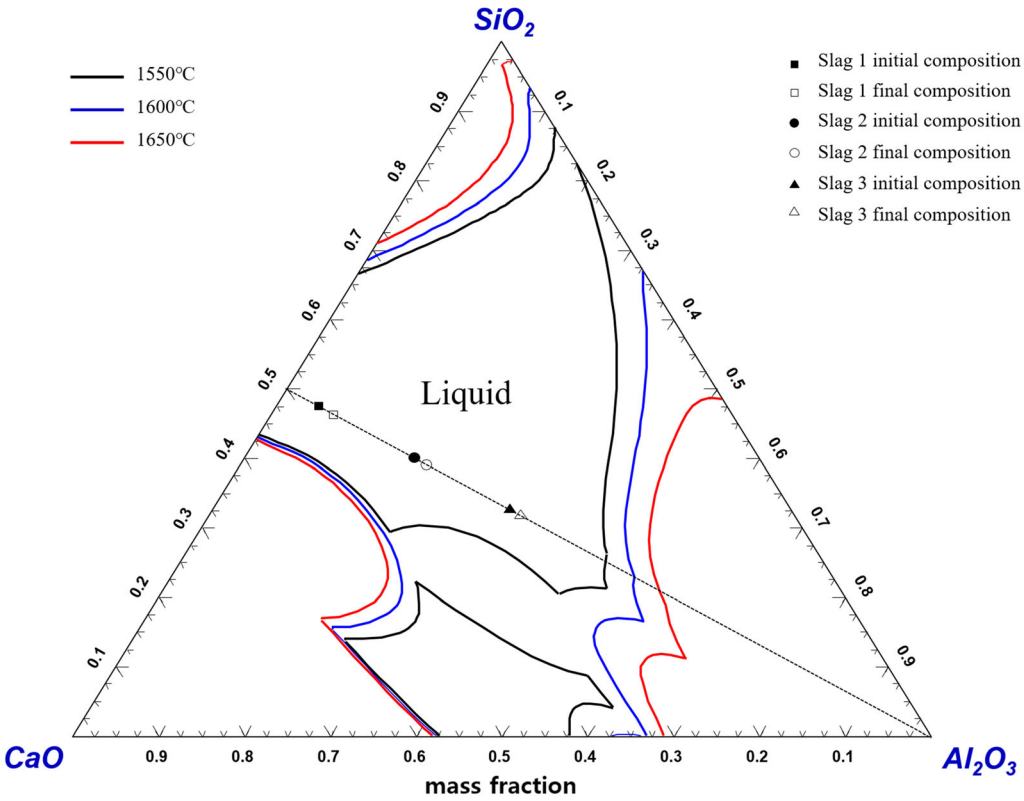

Fig. 1—Phase diagram of the CaO–Al_2O_3–SiO_2 slag a system.

phenomenon in mold slags and crystallization behavior of mold slags.[22,23] However, Kim *et al.*[19] were the first to begin dissolution studies using the SHTT. They reported that the $MgAl_2O_4$ phase was clearly observed at the interface between the MgO particles and CaO–Al_2O_3–SiO_2 slag (containing more than 20 pct Al_2O_3) through the quenched specimen. Wang *et al.*[20] investigated the dissolution of Al_2O_3 inclusions in ladle slags with different CaO/Al_2O_3 ratios with the SHTT. Chen *et al.*[21] studied the effect of slag basicity and Li_2O content on the dissolution behavior of Al_2O_3 in mold flux using the SHTT. Compared to other method, the SHTT can be observed the dissolution phenomenon between inclusions and slags in real time. This method can get very clear images through a high-resolution camera. It was also possible to perform various analyses on quenched specimens through rapid quenching. Although previous studies have been conducted, but no study has been focused on Al_2O_3 activity in the slag. In this study, we were investigating the dissolution phenomenon with the SHTT by changing the alumina activity in the slag at various temperatures.

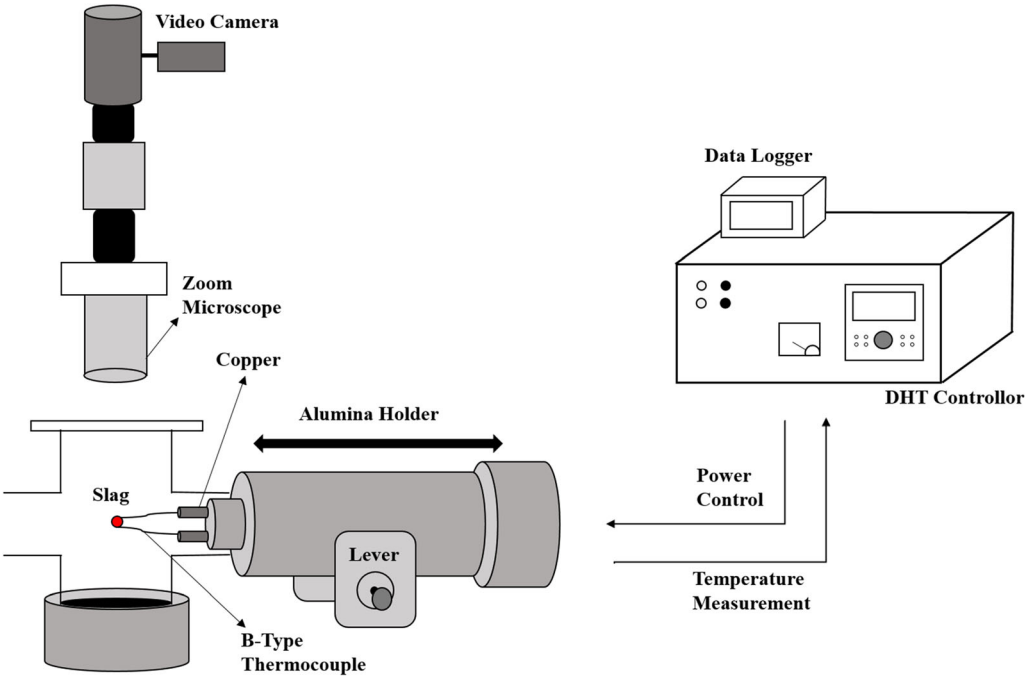

Fig. 2—Schematic diagram of single hot thermocouple technique apparatus.

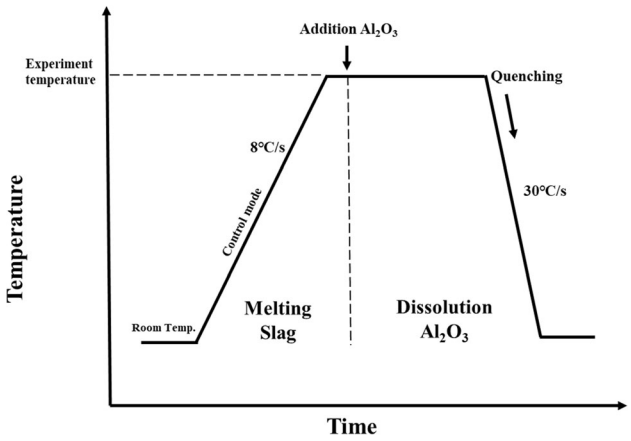

Fig. 3—Experimental procedure of Al_2O_3 dissolution.

II. EXPERIMENTAL METHOD

Table I shows the composition of the Al_2O_3 sphere. The Al_2O_3 particles were 500 ± 25 μm in diameter (GoodFellow Cambridge Limited, Huntingdon, U.K.). The average weight was 0.25 mg, and the purity of Al_2O_3 was 99.9 pct (3 N).

Table II shows the chemical composition of the slags used in this study. All the slags had a fixed basicity (CaO/SiO_2 ratio) of 1. The content of Al_2O_3 in the slag varied from 5 to 35 pct. The amount of slag used in each experiment was about 10 mg. Chen *et al.*[21] studied the effect of particle size on the experimental reproducibility, and suggested the mass ratio of the particle to molten slag is to be less than about 2 pct. In this study, Al_2O_3 content was changed to be about 2.3 to 2.5 pct. The slags were individually mixed with $CaCO_3$ (99.0 pct), Al_2O_3 (99.5 pct), and SiO_2 (99.5 pct) powders. The CaO powder was prepared by calcining $CaCO_3$ in a horizontal furnace at 1200 °C for 3 hours.

Figure 1 shows that each slag was in the liquid phase at 1550 °C, 1600 °C, and 1650 °C from the $CaO–Al_2O_3–SiO_2$ ternary phase diagram obtained using Factsage$^{7.3TM}$. The compositions of the slags before and after are shown in the phase diagram. The amount of the changed composition of Al_2O_3 in the slag was 2.3 wt pct in slag 1, 2 wt pct in slag 2, and 1.6 wt pct in slag 3 as can be seen in Figure 1.

Figure 2 shows a schematic of the apparatus equipped with a high-magnification microscope that can observe the molten slags in real time at experimental temperatures. The SHTT can make a simultaneous measurement of the temperature while a thermocouple is being heated. The +, − poles of the B-type thermocouples were welded to make an oval shape, and the slag powder was mounted on the tip to melt the slag.

Figure 3 shows the procedure of the Al_2O_3 dissolution experiment. Before proceeding with the dissolution experiment, the slag powder is placed on the thermocouple tip and the temperature of the thermocouple is raised by 8 °C/s to the experiment temperature in the control mode. The experiment temperature was maintained until the slag powder was completely melted and all bubbles in the slags disappeared. After inserting the Al_2O_3 particles into the transparent molten slag, a dissolution image was taken through a high-magnification microscope within 3 seconds. In this process, with the insertion of Al_2O_3 particles, a temperature drop could occur, but the temperature is recovered by the power controlling system. We analyzed the images of the dissolution process to obtain the particle diameter with time through image analysis software (Image J). To

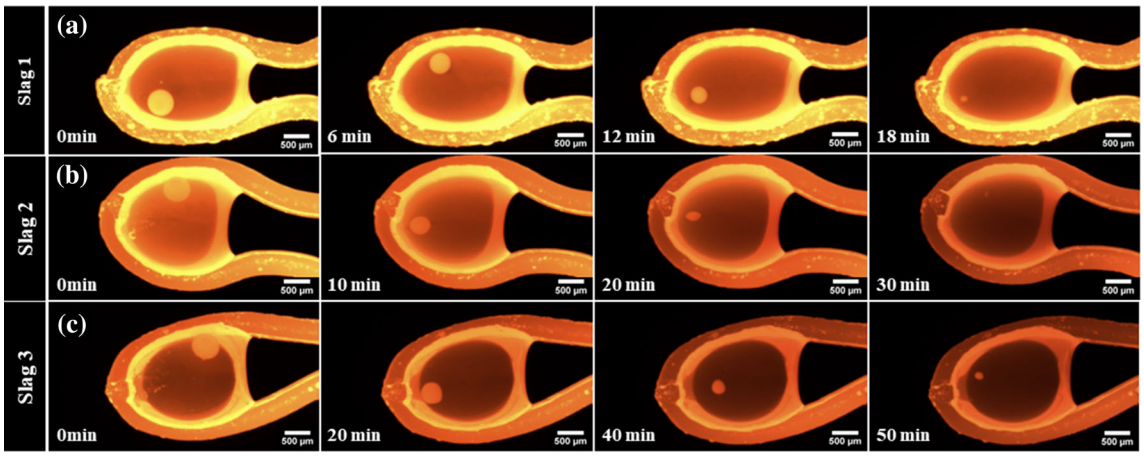

Fig. 4—Al_2O_3 optical image as a function of time measured by video camera at 1550 °C in (*a*) slag 1, (*b*) slag 2, and (*c*) slag 3.

Table III. Dissolution Time of Al_2O_3 Particles Under Each Condition

	1550 °C	1600 °C	1650 °C
Slag 1	1338 s	742 s	571 s
Slag 2	2255 s	1036 s	761 s
Slag 3	3634 s	1515 s	1172 s

observe the particle/slag interfacial phenomenon, the samples were quenched at a cooling rate of 30 °C/s. The polished specimen was analyzed by the Scanning Electron Microscope (SEM).

III. RESULTS

To understand the dissolution behavior of Al_2O_3 particles, we conducted the experiment with SHTT by changing the content of Al_2O_3 in the slag and by changing the temperature from 1550 °C to 1650 °C.

A. *The Dissolution Rate of Al_2O_3 as the Activity of Al_2O_3 in Slag*

Figure 4 shows the Al_2O_3 dissolution optical images over time, and (a), (b), and (c) show the dissolved Al_2O_3 in slag 1 (5 pct Al_2O_3), 2 (20 pct Al_2O_3), and 3 (35 pct Al_2O_3), respectively. The optical images clearly observed that the radius of the Al_2O_3 particles decreases as a function of time in all the slags. Table III shows the total dissolution time taken from insertion to dissolution at each slag and the given temperatures. The total Al_2O_3 dissolution time was 1338 seconds at 1550 °C and 571 seconds at 1650 °C in slag 1. Slag 3 with increased Al_2O_3 content was 3634 seconds at 1550 °C and 1172 seconds at 1650 °C. Figure 5 shows the change in the radius of the particle with time using Image J analysis. The results show that the higher the Al_2O_3 content of the slag, the slower the Al_2O_3 particle dissolution rate. It can be seen that as the temperature increases, the dissolution rate of the Al_2O_3 particles increases. The dissolution rate on slag 3 rather than either slag 1 or slag 2 was more delayed. In particular, the dissolution rate of slag 3 was slower than the one of slag 1 by about 3 times at 1550 °C.

B. *The Particle/Slag Interface Analysis by SEM*

To better understand the dissolution behavior of Al_2O_3 particles in liquid slags, we quenched the liquid slags containing Al_2O_3 particles. The maximum quenching condition was at a rate of 30 °C/s which acquired for turning off the power of the apparatus. A cross-section of the quenched sample was observed through SEM. Figure 6 shows the SEM images at the given time for each slag. The particle radius at the particle/slag interface during the dissolution of Al_2O_3 was reduced over time without a reaction layer. Park *et al.*[24] reported that a reaction product was formed at the particle surface depending on the slag composition. In the slag composition of this study, the SEM images confirmed that no reaction product was formed at the particle surface. Therefore, the dissolution rate was not delayed by the reaction product in this experimental condition.

C. *The Particle Rotation During the Dissolution*

The particle rotation has been reported using the CSLM by Valdez[12] and Liu *et al.*[13]. The particle rotation phenomenon was also observed in the SHTT experiment, which is shown in Figure 7. Figure 7(a) shows the dissolution curve of Al_2O_3 particles in slag 1

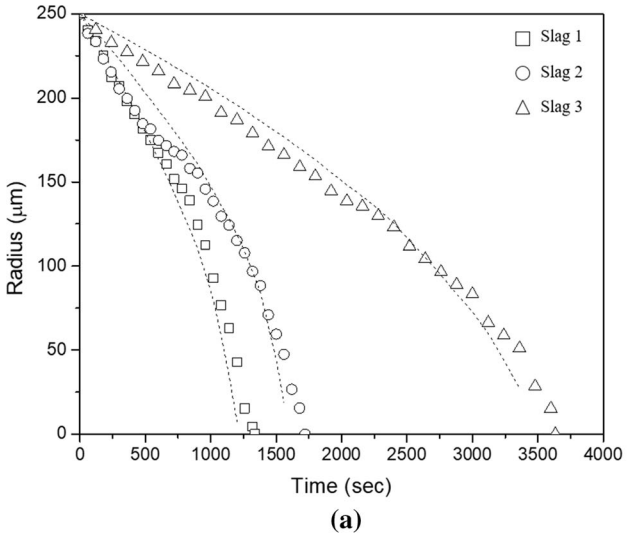

(a)

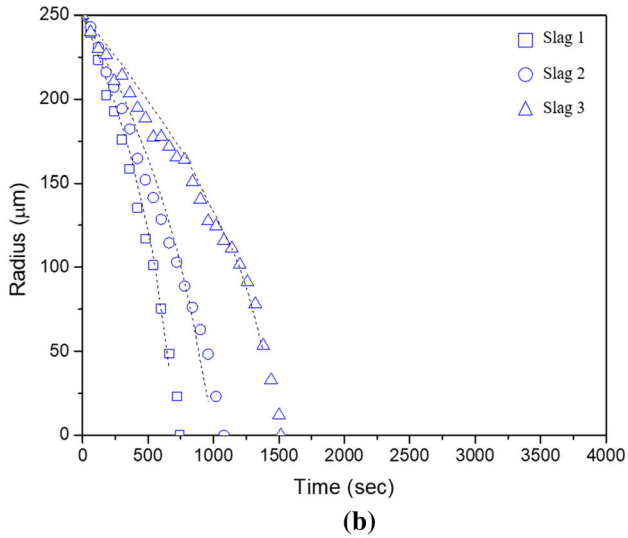

(b)

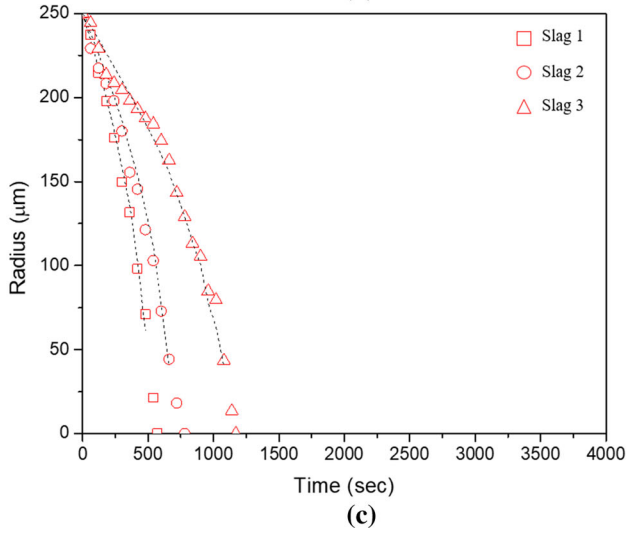

(c)

Fig. 5—Al_2O_3 particle dissolution results at 1550 °C, 1600 °C, and 1650 °C and comparison between the calculation dissolution curves through Eqs. [6], [8], and [9] and the experimental data. (*a*) Slag 1, (*b*) Slag 2, and (*c*) Slag 3.

at 1550 °C, and the magnified plot is described in Figure 7(b). The particle rotation was observed during all the experiments. The cycle of a particle rotation was measured for each experiment as shown in Table IV.

The particle rotation affects the dissolution kinetics. According to Yan *et al.*[25], a kinetic model must be incorporated with a fluid flow due to the rotation and a Peclet number is used. In this study, the kinetic model related to a fluid flow was also needed for clearly understanding the dissolution behavior of particles. It might be due to Marangoni flow and/or natural convection which can be generated by inbalance of alumina concentration at the interface between the slag and particle during dissolution.[16]

IV. DISCUSSION

A. *A Kinetic Model Related to a Fluid Flow*

Most researchers used the shrinking core model to predict the particle dissolution curve. During the dissolution process, the mass change of a dissolving sphere can be expressed in Eq. [1] [25]:

$$dN_P = \rho_p dV = \rho_p 4\pi R^2 dR \qquad [1]$$

where N_P and V are the mass and volume of a dissolving particle; ρ_p is the densities of the dissolving particle; R is the radius of the sphere. This mass change with time equals the mass flux across the boundary layer when the mass transfer is the rate-controlling step, and the following equation applies:

$$-\frac{4\rho_p R^2 dR}{dt} = 4\pi R^2 k \Delta C \qquad [2]$$

where k is the reaction rate constant; ΔC is the concentration difference between the dissolving sphere and slag. When a flow condition is flow fluid, it can access via the Pe number and Re number as follows:

$$\mathrm{Pe} = \frac{2RU}{D}, \quad \mathrm{Re} = \frac{2R\rho_s U}{\eta} \qquad [3]$$

where U is the fluid flow speed around the particle, η is the viscosity of the liquid slag; D is the diffusion coefficient of alumina in the slag. A Peclet number is a dimensionless number that can relate the effectiveness of mass transport by advection and the effectiveness of mass transport by diffusion.[26] A Reynolds number is the ratio of inertial force and viscous force, and is a dimensionless number that can determine which behavior is dominant in a given flow condition. If the fluid dynamics falls in the Stokes regime,[27] Pe number $\ll 10$, *Re* number $\ll 1$, mass transfer coefficient k approximately equals D/R.[28] Based on the assumption that the fluid flow is the Stokes regime, the previous literature described the dissolution of inclusions using the shrinking core model.

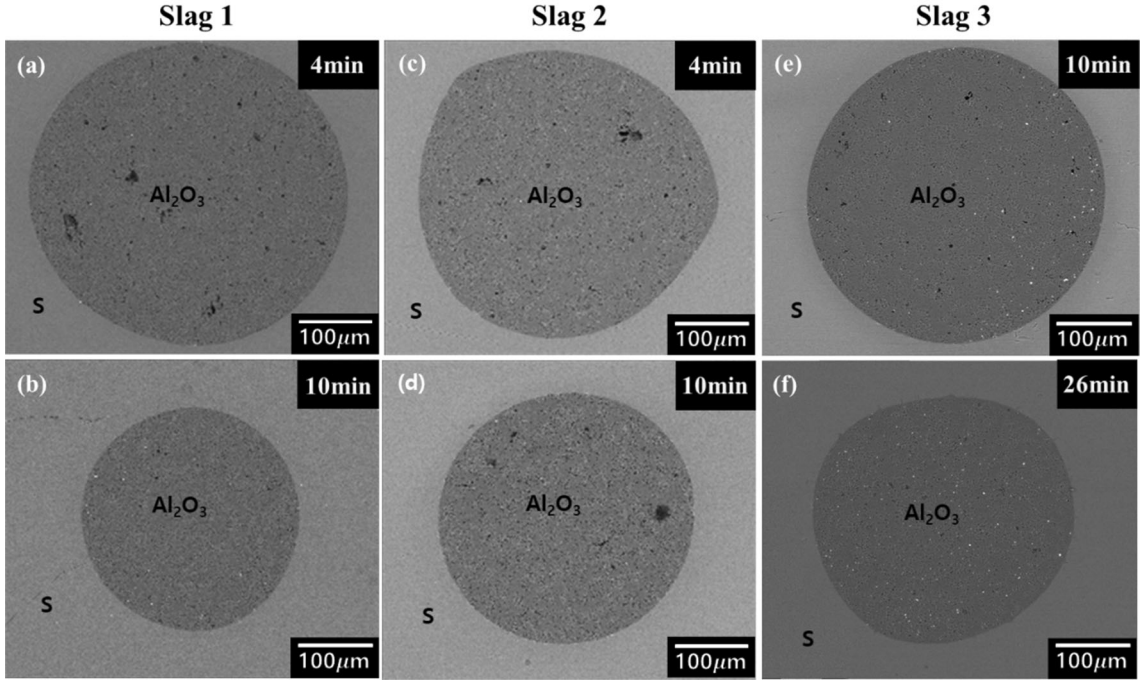

Fig. 6—Al_2O_3 particles cross-section image by SEM at 1550 °C. (S = Slag). (*a*) after 4 min in slag 1, (*b*) after 10 min in slag 1, (*c*) after 4 min in slag 2, (*d*) after 10 min in slag 2, (*e*) after 10 min in slag 3, (*f*) after 26 min in slag 3.

However, the rotation of particles was observed during the dissolution in the SHTT, and the dissolution of particles was affected by the fluid flow at the particle/slag boundary. The flow speed around the particles is not zero, which means that the fluid flow will not be a Stokes regime. Yan *et al.*[25] studied the change of Pe and Re as a function of particle radius with the diffusion coefficient and viscosity. It clearly shows that the condition for Pe << 10 is not satisfied, especially for larger particles. Thus, $k \neq D/R$ would not hold. Instead, the mass transfer has to be directly linked with actual particle size and the fluid dynamics at the particle/slag boundary with Eqs. [4] and [5], to calculate the true dependence of k on particle size:

$$k_s = \frac{D_s\left(4.0 + 1.21\mathrm{Pe}^{2/3}\right)^{1/2}}{2R}, \quad \mathrm{Pe} \leq 10,000 \qquad [4]$$

$$k_s = \frac{1.1 D_s \mathrm{Pe}^{1/3}}{2R}, \quad \mathrm{Pe} \geq 10,000 \qquad [5]$$

Figure 8 compares the calculated dissolution curves using Eqs. [2], [4], and [5] in each slag with the experimental data. The calculated dissolution curve and the experimental data are fitted well, but there was an initial deviation at 1550 °C for slag 2 for slag 3. This may have been due to the acceleration of dissolution when the temperature recovered after insertion of the particle.

The diffusion coefficient can be obtained by calculating the mass transfer coefficient through Eqs. [2], [4], and [5] in Table V. Detailed calculation parameters are listed in Table V. The range of the diffusion coefficient calculated in this study was within the range of 10^{-12} to 10^{-10} m^2/s as suggested by Yan *et al.*[25] However, the diffusion coefficient on slag 3 at 1550 °C decreased to 4.55×10^{-13} m^2/s. The reason may be because the viscosity of slag 3 was higher than other slags. It must be the high viscosity as shown in Table V.

B. *Activation Energy*

We conducted experiments at various temperature conditions to determine the activation energy of Al_2O_3 dissolution. Figure 5 shows that the dissolution rate of the particle increases as the temperature increases. The effect of temperature on the diffusion coefficient can be using the Arrhenius relation represented by Eq. [6]:

$$D = D_0 \cdot \exp\left(-\frac{E_D}{RT}\right) \qquad [6]$$

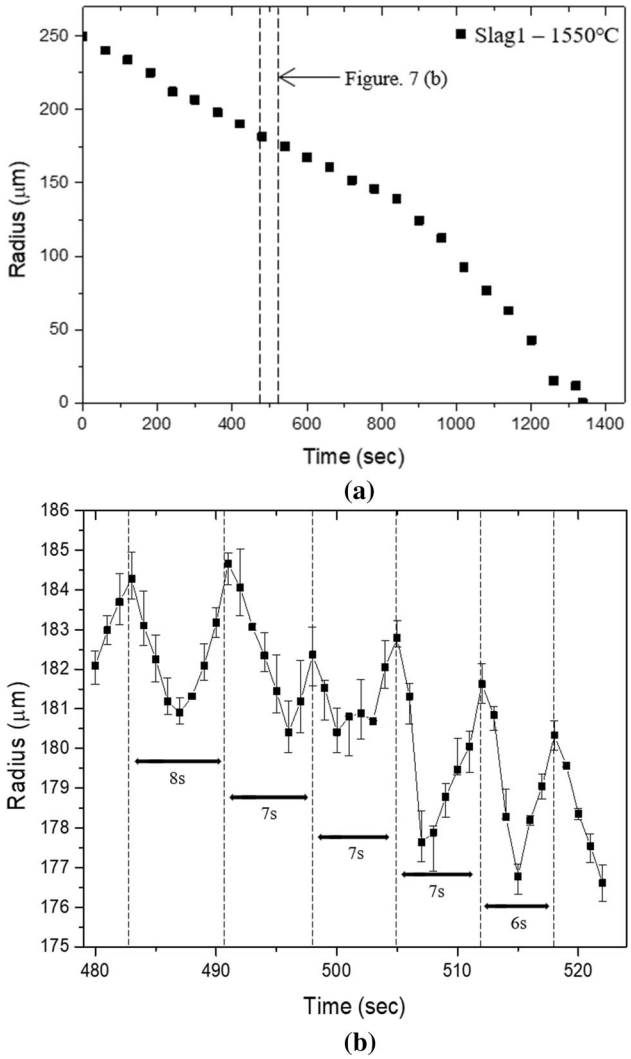

Fig. 7—Particle rotation during dissolution with a period (*a*) Dissolution of Al_2O_3 particle in slag 1 at 1550 °C, (*b*) rotation frequency of Al_2O_3 particle.

Table IV. Rotating Period of Al_2O_3 Particles During Dissolution

	Slag 1	Slag 2	Slag 3
1550 °C	7 s	14 s	23 s
1600 °C	5 s	12 s	21 s
1650 °C	4 s	11 s	17 s

where E_D is the activation energy, R is the gas constant, T is temperature, and D_0 is a constant. Figure 8 shows the natural logarithm of the diffusion coefficient *vs.* $1/T$ (K). Based on the Arrhenius relation, the slope

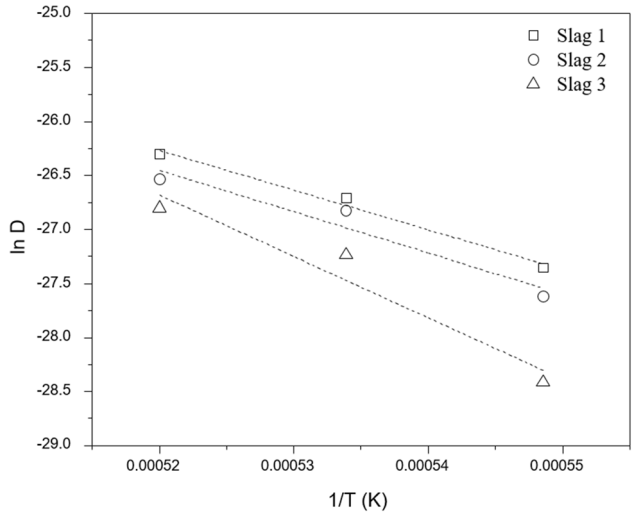

Fig. 8—Determination of activation energy for the diffusion coefficient.

obtained from this figure is indicative of the activation energy for the diffusion. The calculated activation energy is 323 kJ/mole in slag 1, 343 kJ/mole in slag 2, and 486 kJ/mole in slag 3. As the Al_2O_3 activity in the slag increased, the activation energy of diffusion increased due to the dissolution of the driving force.

V. CONCLUSION

We studied the dissolution behavior of Al_2O_3 by changing Al_2O_3 activity in $CaO–Al_2O_3–SiO_2$ slag using a single hot thermocouple technique. The following conclusions can be drawn as below.

1. The dissolution rate of Al_2O_3 decreased with increasing Al_2O_3 activity in slag. The driving force for Al_2O_3 dissolution was the concentration difference of Al_2O_3 between the particle/slag interface and the bulk slag. Decreasing the concentration of Al_2O_3 in slags increased in the dissolution rate.
2. The particle rotation was observed during the dissolution experiment. The dissolution of Al_2O_3 was controlled by mass transfer with a fluid flow. The diffusion coefficient of Al_2O_3 was calculated from 10^{-12} to 10^{-10} m^2/s in a way similar to a previous study. However, we obtained 4.55×10^{-13} m^2/s for 35 pct Al_2O_3 at 1550 °C. It must be the low viscosity.
3. The activation energy of the diffusion was 323 kJ/mole at 5 wt pct Al_2O_3, 343 kJ/mole at 20 wt pct Al_2O_3, and to 486 kJ/mole at 35 wt pct Al_2O_3. It increased with increasing Al_2O_3 activity in slags due to the lower driving force of alumina content.

Table V. Calculated Diffusion Coefficients and Activation Energy in Present Study and Literature Available for Alumina Dissolution

Slag[a]	Temperature (°C)	$\Delta C_{Al_2O_3}$ (mole/m^3)	Slag Density (kg/m^3)	Viscosity (Pa S) (Factsage$^{7.3TM}$)	D(m^2/s)	Activation Energy, Q_D (kJ/mole)	Method[b]	References
1	1650	11,742	2634	0.158	3.77×10^{-12}	323	SHTT	present study
	1600	11,386	2647	0.205	2.51×10^{-12}			
	1550	10,814	2660	0.270	1.32×10^{-12}			
2	1650	7731	2701	0.277	2.99×10^{-12}	343		
	1600	7329	2714	0.373	2.23×10^{-12}			
	1550	6768	2728	0.510	1.01×10^{-12}			
3	1650	3911	2658	0.526	2.29×10^{-12}	486		
	1600	3485	2670	0.750	1.48×10^{-12}			
	1550	2905	2684	1.100	4.55×10^{-13}			
4	1340 to 1550	—	—	—	10^{-13} to 10^{-11}	—	RDM	[5]
5	1500 to 1600	—	—	—	—	288 to 390	RCM	[10]
6	1470 to 1630	—	—	—	10^{-11}	—	CSLM	[13]
7	1477 to 1577	—	—	—	10^{-11} to 10^{-10}	—	CSLM	[16]
8	1600	—	—	—	10^{-12} to 10^{-9}	—	CSLM	[17]

[a]4 to 7 CAS, 8: CASM, A: Al_2O_3, C: CaO, M: MgO, S: SiO_2.
[b]*SHTT* single hot thermocouple technique, *RDM* rotating disk method, *RCM* rotating cylinder method, *CSLM* confocal scanning laser microscopy.

ACKNOWLEDGMENTS

This work was partly supported by Korea Institute of Energy Technology Evaluation and Planning (KETEP) grant (Grant Number 20172010106310), and by Korea Institute for Advancement of Technology (KIAT) grant (Grant Number P0008425) funded by the Ministry of Trade, Industry & Energy (MOTIE), Korea.

REFERENCES

1. P.A.. Thornton: *J. Mater. Sci.*, 1971, vol. 6, pp. 347–56.
2. S.N. Singh: *Metall. Trans.*, 1974, vol. 5, pp. 2165–78.
3. L. Holappa and O. Wijk: in *Treatise on Process Metallurgy*, S. Seetharaman, ed., Elsevier, Boston, 2014, pp. 347–72.
4. S. Sridhar and A.W. Cramb: *Metall. Mater. Trans. B*, 2000, vol. 31B, pp. 406–10.
5. A.R. Cooper and W.D. Kingery: *J. Am. Ceram. Soc.*, 1964, vol. 47, pp. 37–43.
6. J.-Y. Choi, H.-G. Lee, and J.-S. Kim: *ISIJ Int.*, 2002, vol. 42, pp. 852–60.
7. S. Taira, K. Nakashima, and K. Mori: *ISIJ Int.*, 1993, vol. 33, pp. 116–23.
8. X. Yu, R.J. Pomfret, and K.S. Coley: *Metall. Mater. Trans. B*, 1997, vol. 28B, pp. 275–79.
9. W.D. Cho and P. Fan: *ISIJ Int.*, 2004, vol. 44, pp. 229–34.
10. A.-H. Bui, H.-M. Ha, Y.-B. Kang, I.-S. Chung, and H.-G. Lee: *Met. Mater. Int.*, 2005, vol. 11, p. 183.
11. G. Chen, S. He, and Q. Wang: *J. Mater. Sci. Technol.*, 2020, vol. 9, pp. 11311–318.
12. M.K. Prapakorn, A.W. Cramb, and S. Sridhar: *Ironmak. Steelmak.*, 2002, vol. 29, pp. 47–52.
13. J. Liu, F. Verhaeghe, M. Guo, B. Blanpain, and P. Wollants: *J. Am. Ceram. Soc.*, 2007, vol. 90, pp. 3818–24.
14. S.H. Lee, C. Tse, K.W. Yi, P. Misra, V. Chevrier, C. Orrling, S. Sridhar, and A.W. Cramb: *J. Non- Cryst. Solids*, 2001, vol. 282, pp. 41–48.
15. K.W. Yi, C. Tse, J.-H. Park, M. Valdez, A.W. Cramb, and S. Sridhar: *Scand. J. Metall.*, 2003, vol. 32, pp. 177–84.
16. B.J. Monaghan and L. Chen: *Steel Res. Int.*, 2005, vol. 76, pp. 348–54.
17. S. Michelic, J. Goriupp, S. Feichtinger, Y.B. Kang, C. Bernhard, and J. Schenk: *Steel Res. Int.*, 2016, vol. 87, pp. 57–67.
18. H. Abdeyazdan, N. Dogan, R.J. Longbottom, M.A. Rhamdhani, M.W. Chapman, and B.J. Monaghan: *Advanced Real Time Imaging*, Springer, Cham, 2019, pp. 61–73.
19. Y. Kim, Y. Kashiwaya, and Y. Chung: *Ceram. Int.*, 2020, vol. 46, pp. 6205–11.
20. R. Wang, Y. Bao, Y. Li, T. Li, and D. Chen: *J. Iron Steel Res. Int.*, 2017, vol. 24, pp. 579–85.
21. F. Chen, P. Tang, G. Wen, L. Yu, and S. Gu: *ISIJ Int.*, 2021, vol. 61, pp. 200–208.
22. Y. Kashiwaya, C.E. Cicutti, A.W. Cramb, and K. Ishii: *ISIJ Int.*, 1998, vol. 38, pp. 348–56.
23. Y. Kashiwaya, C.E. Cicutti, and A.W. Cramb: *ISIJ Int.*, 1998, vol. 38, pp. 357–65.
24. J.-H. Park, I.-H. Jung, and H.-G. Lee: *ISIJ Int.*, 2006, vol. 46, pp. 1626–34.
25. P. Yan, B.A. Webler, P.C. Pistorius, and R.J. Fruehan: *Metall. Mater. Trans. B*, 2015, vol. 46B, pp. 2414–18.
26. C. W. Fetter, T. B. Boving, D. K. Kreamer: Upper Saddle River, NJ: Prentice Hall, 1999.
27. O. Levenspiel: *Chemical Reaction Engineering*, 3rd ed., Wiley, New York, 1999.
28. D. Wang, X. Li, H. Wang, Y. Mi, M. Jiang, and Y. Zhang: *J. Non-Cryst. Solids*, 2012, vol. 358, pp. 1196–1201.